

Generalized likelihood ratio detector for forward scattering detection in uncertain shallow-water environments

Jiahui Luo(罗嘉辉), Chao Sun(孙超), Mingyang Li(李明杨), and Shaodong Zhang(张少东)
Citation: Chin. Phys. B, 2026, 35 (**5**): 054303. DOI: 10.1088/1674-1056/ae118f
http://cpb.iphy.ac.cn; http://iopscience.iop.org/cpb

What follows is a list of articles you may be interested in

Boundary effects on modal shape in deep ocean via non-integer order parabolic cylinder functions

Jian-Kang Zhan(詹建康), Sheng-Chun Piao(朴胜春), and Li-Jia Gong(龚李佳)
Chin. Phys. B, 2026, 35 (**2**): 024303. DOI: 10.1088/1674-1056/ae1b7c

Single broadband source depth estimation using Stokes parameters in shallow water

Yizheng Wei(韦宜政), Chao Sun(孙超), Lei Xie(谢磊), and Mingyang Li(李明杨)
Chin. Phys. B, 2026, 35 (**2**): 024301. DOI: 10.1088/1674-1056/adee01

A WKB method based on parabolic cylinder function for very-low-frequency sound propagation in deep ocean

Jian-Kang Zhan(詹建康), Sheng-Chun Piao(朴胜春), Li-Jia Gong(龚李佳), Yang Dong(董阳), Yong-Chao Guo(郭永超), and Guang-Xue Zheng(郑广学)
Chin. Phys. B, 2025, 34 (**3**): 034301. DOI: 10.1088/1674-1056/ada886

Method for measuring the low-frequency sound power from a complex sound source based on sound-field correction in a non-anechoic tank

Hongzhe Xu(徐宏哲), Qi Li(李琪), Rui Tang(唐锐), and Dajing Shang(尚大晶)
Chin. Phys. B, 2023, 32 (**5**): 054303. DOI: 10.1088/1674-1056/acb75c

Simultaneous detection of the acoustic-field aberration and Doppler shift in forward acoustic scattering

Chuan-Lin He(何传林), Kun-De Yang(杨坤德), Yuan-Liang Ma(马远良), Bo Lei(雷波)
Chin. Phys. B, 2017, 26 (**1**): 014301. DOI: 10.1088/1674-1056/26/1/014301

Generalized likelihood ratio detector for forward scattering detection in uncertain shallow-water environments

Jiahui Luo(罗嘉辉)[1,2], Chao Sun(孙超)[1,2], Mingyang Li(李明杨)[1,2,†], and Shaodong Zhang(张少东)[3]

[1] *School of Marine Science and Technology, Northwestern Polytechnical University, Xi'an* 710072, *China*
[2] *Key Laboratory of Ocean Acoustic and Sensing, Ministry of Industry and Information Technology, Northwestern Polytechnical University, Xi'an* 710072, *China*
[3] *Marine Design and Research Institute of China, Shanghai* 200011, *China*

(Received 1 August 2025; revised manuscript received 22 September 2025; accepted manuscript online 10 October 2025)

Forward scattering detection in shallow-water environments presents many challenges, particularly the issues of environmental uncertainties and direct blast, which is an intense sound wave that propagates directly from the source to the receiver without interaction with the target. In this paper, we account for environmental uncertainties and extend the generalized likelihood ratio detector (GLRD) for forward scattering detection in a known environment to uncertain environments. In a suitable bistatic sonar configuration where the source is positioned on the broadside of a large aperture horizontal linear array (HLA), the GLRD exhibits good resistance to direct blast. Moreover, the GLRD demonstrates a certain degree of robustness against environmental uncertainties, particularly when the sampling uncertainty sets of the direct blast/signal wavefront are large enough — including both the real direct blast wavefront and the real signal wavefront. Despite facing the challenge of direct blast in forward scattering detection, the GLRD still performs well in this scenario and demonstrates its effectiveness as a method for forward scattering detection in uncertain shallow-water environments.

Keywords: forward scattering detection, uncertain environments, generalized likelihood ratio detector (GLRD), horizontal linear array (HLA)

PACS: 43.30.+m, 43.20.Fn, 43.30.Vh, 43.60.Bf

DOI: 10.1088/1674-1056/ae118f **CSTR:** 32038.14.CPB.ae118f

1. Introduction

When a sound wave encounters a target, part of the wave is deflected backward, while the wave propagating forward also changes. The difference between this actual forward-propagating wave and the undisturbed wave, which would be present if the target were not there, is defined as the forward scattering wave.[1] If the target is very large compared with the sound wavelength, as is often the case in a bistatic sonar system, the intensity of the forward scattering wave is significantly higher than that of the backward scattering wave[2,3] typically exceeding 10 dB. This advantage is quite attractive for certain detection scenarios and may improve detection performance. However, forward scattering detection faces additional challenges, particularly caused by the direct blast,[4] which is an intense sound wave transmitted by the source and propagating directly to the receiver without interaction with the target. The direct blast impinges on the receiver simultaneously with the forward scattering wave and from the same direction. This makes it difficult to distinguish them in time-domain or in angle-domain, posing significant challenges for detection.

Resulting from an interference effect between the direct blast and the forward scattering wave, a transient temporal and spatial acoustic aberration may occur in the received data.[5–8] Many researches have been developed to extract and enhance this acoustic aberration for detection. Song *et al.* observed an increase in sidelobe levels around the focal zone caused by target crossing using the time-reversal mirror.[9] Sabra *et al.* developed a coherent processing scheme based on principal component analysis of the stable portion of the recorded waveform.[10] When a target crosses the source-receiver baseline, the variation in the second principal component can exceed 10 dB. Lei *et al.* proposed using an adaptive filter with weights trained on received data in the absence of the target, to suppress the direct blast and extract acoustic aberration, thereby successfully achieving forward scattering detection.[11–13] However, due to oceanographic phenomena[14,15] such as tides, sea swells, internal waves, fronts, and vortices, the shallow water is temporally and spatially variable, exhibiting significant environmental uncertainties.[16–18] These environmental variations may mask acoustic aberrations or lead to the converged weights no longer applicable for detection.

From the perspective of statistical signal processing, forward scattering detection in uncertain shallow-water environments is essentially a signal detection problem under intense interference (i.e., the direct blast) and unknown environmental parameters conditions. The generalized likelihood ratio

†Corresponding author. E-mail: mingyang.li@nwpu.edu.cn

© 2026 Chinese Physical Society and IOP Publishing Ltd. All rights, including for text and data mining, AI training, and similar technologies, are reserved.

detector (GLRD) is commonly used to handle these detection problems with unknown parameters[19–22] and exhibits good performance. Wang *et al.* proposed an interference and environmental-uncertainties-constrained generalized likelihood ratio detector with a horizontal linear array (HLA) to address detection problems in the presence of interference in uncertain shallow-water environments.[23] With prior knowledge of the interference direction, this method exhibits robust performance in deviation from the interference bearing; however, it fails at the interference bearing itself, which is the focus of forward scattering detection.

For a bistatic sonar system, not only the bearing of the source but also its range and depth are known *a priori*.[24] This prior knowledge reduces the uncertainties associated with the source compared to the target, whose position is unknown. Additionally, the source and the target are similar in bearing but differ in range. This difference in range makes it feasible to achieve forward scattering detection.

In this paper, we aim to detect a target that crosses the baseline connecting the source and the horizontal linear array. To address the performance degradation of the GLRD in a known environment caused by environmental parameter mismatches, we account for environmental uncertainties and translate them into wavefront uncertainties. Subsequently, by estimating the signal/direct blast wavefronts using maximum likelihood, we extend the GLRD for forward scattering detection in a known environment to uncertain environments. We analyze its performance in uncertain shallow-water environments and derive its deflection coefficient, which effectively represents its performance. Since the scattering characteristic of a non-cooperative target is usually unknown, an approximate signal model is used to replace the real forward scattering signal for constructing detectors. Additionally, we demonstrate that the direct blast can be effectively suppressed under suitable bistatic sonar configurations. As a result, the forward scattering signal allows for detection even in the presence of intense direct blast in uncertain shallow-water environments.

The paper is organized as follows. In Section 2, the uncertainties in forward scattering detection problem are analyzed. In Section 3, the test statistic of the GLRD under the interference background is derived. We analyze its performance by simulations in Section 4 and demonstrate its effectiveness using experiment data in Section 5. Finally, a conclusion is presented in Section 6.

2. Forward scattering detection problem in uncertain shallow-water environments

2.1. Forward scattering signal model based on the HLA

Forward scattering signal specifically refers to the sound wave scattered in a similar direction relative to the incident wave. With the highest target strength (TS), this forward scattering signal, resulting from the reflection and diffraction of the incident wave by the target, exhibits high intensity and allows for improved detection performance.

Figure 1 shows the configuration of the bistatic sonar, where $z_{\rm s}$, $z_{\rm t}$ and $z_{\rm r}$ represent the depth of the source, the target, and the N-element HLA, respectively; $r_{{\rm sr}_n}$, $r_{{\rm tr}_n}$ and $r_{\rm st}$ represent the horizontal distances of the source and target relative to the nth element, as well as the horizontal distance between the source and the target, respectively; φ_0 denotes the incident azimuth angle between the source and the target, and φ_n denotes the scattered azimuth angle between the nth element and the target. When $\phi_0 \approx 0$ and $\phi_n \approx \pi$, the scattered signal specifically refers to the forward scattering signal, which is the primary focus of this paper.

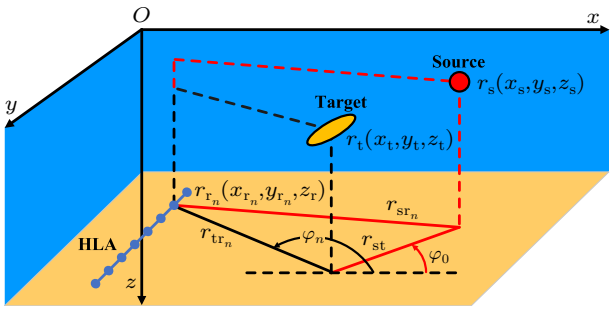


Fig. 1. Geometric relationship between the source, the target, and the HLA (the plane of xOy represents the sea surface, z represents the depth).

In detection scenarios with a point source of unit strength, the scattered signals received by the nth element can be denoted by[25]

$$\begin{aligned}\phi_{\rm s}(\boldsymbol{r}_{{\rm r}_n}) \approx \frac{4\pi}{k}\sum_{m=1}^{M}\sum_{m'=1}^{M}\Big\{&A_{m'}(\boldsymbol{r}_{\rm s})\Big[A_m(\boldsymbol{r}_{{\rm r}_n})\\ &\times S(\pi-\theta_m,\phi_n;\pi-\theta_{m'},\phi_0)-B_m(\boldsymbol{r}_{{\rm r}_n})\\ &\times S(\theta_m,\phi_n;\pi-\theta_{m'},\phi_0)\Big]-B_{m'}(\boldsymbol{r}_{\rm s})\\ &\times\Big[A_m(\boldsymbol{r}_{{\rm r}_n})S(\pi-\theta_m,\phi_n;\theta_{m'},\phi_0)\\ &-B_m(\boldsymbol{r}_{{\rm r}_n})S(\theta_m,\phi_n;\theta_{m'},\phi_0)\Big]\Big\},\end{aligned} \tag{1}$$

where

$$\begin{aligned}A_{m'}(\boldsymbol{r}_{\rm s}) &= \frac{{\rm j}\psi_{m'}(z_{\rm s})N_{m'}{\rm e}^{{\rm j}(k_{rm'}r_{\rm st}+k_{zm'}z_{\rm t}-\pi/4)}}{\rho_{\rm w}\sqrt{8\pi k_{rm'}r_{\rm st}}},\\ B_{m'}(\boldsymbol{r}_{\rm s}) &= \frac{{\rm j}\psi_{m'}(z_{\rm s})N_{m'}{\rm e}^{{\rm j}(k_{rm'}r_{\rm st}-k_{zm'}z_{\rm t}-\pi/4)}}{\rho_{\rm w}\sqrt{8\pi k_{rm'}r_{\rm st}}},\\ A_m(\boldsymbol{r}_{{\rm r}_n}) &= \frac{{\rm j}\psi_m(z_{\rm r})N_m{\rm e}^{{\rm j}(k_{rm}r_{{\rm tr}_n}+k_{zm}z_{\rm t}-\pi/4)}}{\rho_{\rm w}\sqrt{8\pi k_{rm}r_{{\rm tr}_n}}},\\ B_m(\boldsymbol{r}_{{\rm r}_n}) &= \frac{{\rm j}\psi_m(z_{\rm r})N_m{\rm e}^{{\rm j}(k_{rm}r_{{\rm tr}_n}-k_{zm}z_{\rm t}-\pi/4)}}{\rho_{\rm w}\sqrt{8\pi k_{rm}r_{{\rm tr}_n}}};\end{aligned} \tag{2}$$

where $\psi_m(z_{\rm s})$ and $\psi_m(z_{\rm r})$ are the mth mode depth functions at the depths of $z_{\rm s}$ and $z_{\rm r}$, respectively, and k_{rm} is the associated horizontal wavenumber; k is the wavenumber at the target

depth and k_{zm} is the associated vertical wavenumber that satisfies $k_{zm}=\sqrt{k^2-k_{rm}^2}$; $\theta_m=\cos^{-1}(k_{zm}/k)$ is the mth mode angle relative to the positive z-axis; N_m is a normalization constant that satisfies $\psi_m(z_{\rm t})=N_m\left(\mathrm{e}^{\mathrm{j}k_{zm}z_{\rm t}}-\mathrm{e}^{-\mathrm{j}k_{zm}z_{\rm t}}\right)$; M is the number of propagating modes excited in the environment and $\rho_{\rm w}$ is the water density; $S(\theta_m,\varphi_n;\theta_{m'},\varphi_0)$ is the scattering function, determining the target scattering characteristic within the space.

High-order normal modes dissipate rapidly in the far field in shallow-water environments, and low-order normal modes dominate. The mode angles of these low-order normal modes are close to $\pi/2$. Therefore, one further approximation can be made that $\theta_m\approx\pi/2$ and then Eq. (1) reduces to[25,26]

$$\begin{aligned}\phi_{\rm s}(\boldsymbol{r}_{{\rm r}_n}) &\approx \frac{\mathrm{j}}{2\rho_{\rm w}^2k}S\left(\frac{\pi}{2},\varphi_n;\frac{\pi}{2},\varphi_0\right)\sum_{m'=1}^{M}\psi_{m'}(z_{\rm s})\psi_{m'}(z_{\rm t})\\ &\quad\times\frac{\mathrm{e}^{\mathrm{j}k_{rm'}r_{\rm st}}}{\sqrt{k_{rm'}r_{\rm st}}}\sum_{m=1}^{M}\psi_m(z_{\rm t})\psi_m(z_{\rm r})\frac{\mathrm{e}^{\mathrm{j}k_{rm}r_{{\rm tr}_n}}}{\sqrt{k_{rm}r_{{\rm tr}_n}}}\\ &=\frac{1}{4\pi}\frac{S\left(\frac{\pi}{2},\varphi_n;\frac{\pi}{2},\varphi_0\right)}{k}g(\boldsymbol{\Phi},\boldsymbol{r}_{\rm s},\boldsymbol{r}_{\rm t})\,g(\boldsymbol{\Phi},\boldsymbol{r}_{\rm t},\boldsymbol{r}_{{\rm r}_n}),\end{aligned}\tag{3}$$

where $\boldsymbol{\Phi}$ is an environmental vector, including all environmental parameters, such as water depth, surface sound speed, bottom sound speed, etc; $g(\boldsymbol{\Phi},\boldsymbol{r}_{\rm s},\boldsymbol{r}_{\rm t})$ and $g(\boldsymbol{\Phi},\boldsymbol{r}_{\rm t},\boldsymbol{r}_{{\rm r}_n})$ represent the acoustic transfer functions between the transmitting source and the target, and that between the target and the nth element, respectively, which can be denoted by[27]

$$\begin{aligned}g(\boldsymbol{\Phi},\boldsymbol{r}_{\rm s},\boldsymbol{r}_{\rm t})&=\frac{\sqrt{2\pi}\mathrm{e}^{\mathrm{j}\pi/4}}{\rho_{\rm w}}\sum_{m=1}^{M}\psi_m(z_{\rm s})\psi_m(z_{\rm t})\frac{\mathrm{e}^{\mathrm{j}k_{rm}r_{\rm st}}}{\sqrt{k_{rm}r_{\rm st}}},\\ g(\boldsymbol{\Phi},\boldsymbol{r}_{\rm t},\boldsymbol{r}_{{\rm r}_n})&=\frac{\sqrt{2\pi}\mathrm{e}^{\mathrm{j}\pi/4}}{\rho_{\rm w}}\sum_{m=1}^{M}\psi_m(z_{\rm t})\psi_m(z_{\rm r})\frac{\mathrm{e}^{\mathrm{j}k_{rm}r_{{\rm tr}_n}}}{\sqrt{k_{rm}r_{{\rm tr}_n}}}.\end{aligned}\tag{4}$$

For detection scenarios where the target is far from the HLA, the scattered azimuth angles are approximately equal, i.e., $\varphi_1\approx\cdots\approx\varphi_N$. Assuming the acoustic pressure excited by the source at a distance of 1 m is a, corresponding to a source strength of $4\pi a$, the forward scattering signal received by the HLA can be approximated as

$$\begin{aligned}\boldsymbol{s}_{\rm target}&\approx a\frac{S\left(\frac{\pi}{2},\varphi_1;\frac{\pi}{2},\varphi_0\right)}{k}g(\boldsymbol{\Phi},\boldsymbol{r}_{\rm s},\boldsymbol{r}_{\rm t})\,\boldsymbol{g}(\boldsymbol{\Phi},\boldsymbol{r}_{\rm t},\boldsymbol{r}_{\rm r})\\ &=b\boldsymbol{g}(\boldsymbol{\Phi},\boldsymbol{r}_{\rm t},\boldsymbol{r}_{\rm r}),\end{aligned}\tag{5}$$

where $\boldsymbol{s}_{\rm target}=[\phi_{\rm s}(\boldsymbol{r}_{{\rm r}_1}),\ldots,\phi_{\rm s}(\boldsymbol{r}_{{\rm r}_N})]^{\rm T}$ is a frequency-domain received data snapshot; the superscript T denotes the transpose operation; $\boldsymbol{g}(\boldsymbol{\Phi},\boldsymbol{r}_{\rm t},\boldsymbol{r}_{\rm r})=[g(\boldsymbol{\Phi},\boldsymbol{r}_{\rm t},\boldsymbol{r}_{{\rm r}_1}),\ldots,g(\boldsymbol{\Phi},\boldsymbol{r}_{\rm t},\boldsymbol{r}_{{\rm r}_N})]^{\rm T}$ is an $N\times1$ column vector, representing the signal wavefront that is an acoustic pressure vector received by the HLA. The forward scattering signal received by the HLA in the far field is approximated as a signal radiated by a non-directional source that transmits an unknown complex-valued signal b, since $S\left(\frac{\pi}{2},\varphi_1;\frac{\pi}{2},\varphi_0\right)$ is unknown for a non-cooperative target.

In forward scattering detection, the HLA receives not only the forward scattering signal but also the direct blast. This direct blast, an intense acoustic wave directly from the source without interaction with the target, can be denoted by

$$\boldsymbol{s}_{\rm source}=a\boldsymbol{g}(\boldsymbol{\Phi},\boldsymbol{r}_{\rm s},\boldsymbol{r}_{\rm r}),\tag{6}$$

where $\boldsymbol{g}(\boldsymbol{\Phi},\boldsymbol{r}_{\rm s},\boldsymbol{r}_{\rm r})=[g(\boldsymbol{\Phi},\boldsymbol{r}_{\rm s},\boldsymbol{r}_{{\rm r}_1}),\ldots,g(\boldsymbol{\Phi},\boldsymbol{r}_{\rm s},\boldsymbol{r}_{{\rm r}_N})]^{\rm T}$ is the direct blast wavefront; $g(\boldsymbol{\Phi},\boldsymbol{r}_{\rm s},\boldsymbol{r}_{{\rm r}_n})$ represents the acoustic transfer function between the source and the nth element that can be denoted by[27]

$$g(\boldsymbol{\Phi},\boldsymbol{r}_{\rm s},\boldsymbol{r}_{{\rm r}_n})=\frac{\sqrt{2\pi}\mathrm{e}^{\mathrm{j}\pi/4}}{\rho_{\rm w}}\sum_{m=1}^{M}\psi_m(z_{\rm s})\psi_m(z_{\rm r})\frac{\mathrm{e}^{\mathrm{j}k_{rm}r_{{\rm sr}_n}}}{\sqrt{k_{rm}r_{{\rm sr}_n}}}.\tag{7}$$

The forward scattering signal presents a similar expression to the direct blast but with a different wavefront resulting from the difference in positions of the source and the target, and its amplitude b is unknown because the scattering characteristics of a non-cooperative target is unknown. This difference in wavefronts allows for the detection of a target even in the presence of the direct blast.

2.2. Environmental uncertainties in forward scattering detection

From signal models, Eqs. (5) and (6), the forward scattering detection in shallow-water environments is approximated as a detection problem in the presence of an unknown amplitude interference, which can be formulated as the following binary hypothesis test problem:

$$\begin{aligned}\mathcal{H}_0&:\boldsymbol{x}=\boldsymbol{g}(\boldsymbol{\Phi},\boldsymbol{r}_{\rm s})a+\boldsymbol{w},\\ \mathcal{H}_1&:\boldsymbol{x}=\boldsymbol{g}(\boldsymbol{\Phi},\boldsymbol{r}_{\rm s})a+\boldsymbol{g}(\boldsymbol{\Phi},\boldsymbol{r}_{\rm t})b+\boldsymbol{w},\end{aligned}\tag{8}$$

where $\boldsymbol{x}$ is a frequency-domain received data snapshot, including the direct blast and the noise in the null hypothesis $\mathcal{H}_0$, and additionally the forward scattering signal in the alternative hypothesis $\mathcal{H}_1$; $\boldsymbol{g}(\boldsymbol{\Phi},\boldsymbol{r}_{\rm s})$ and $\boldsymbol{g}(\boldsymbol{\Phi},\boldsymbol{r}_{\rm t})$ are the abbreviations of $\boldsymbol{g}(\boldsymbol{\Phi},\boldsymbol{r}_{\rm s},\boldsymbol{r}_{\rm r})$ and $\boldsymbol{g}(\boldsymbol{\Phi},\boldsymbol{r}_{\rm t},\boldsymbol{r}_{\rm r})$, respectively, with the prior known $\boldsymbol{r}_{\rm s}$ and $\boldsymbol{r}_{\rm r}$; a and b are unknown amplitudes of the direct blast and the forward scattering signal, respectively; the background noise vector is assumed to be a spatially complex white Gaussian vector with a prior known noise power σ^2, i.e., $\boldsymbol{w}\sim CN\left(0,\sigma^2\boldsymbol{I}_N\right)$, where $\boldsymbol{I}_N$ is an $N\times N$ identity matrix.

When the ocean environment is precisely known, the target position is the only unknown parameter in acoustic transfer functions. By searching for the target position, the optimal detector for this binary hypothesis test problem can be constructed and the associated test statistic is given by[24]

$$T(\boldsymbol{x})=\max_{\boldsymbol{r}\in\boldsymbol{R}^{1\times3}}\frac{\left\|\boldsymbol{g}^{\rm H}(\boldsymbol{\Phi},\boldsymbol{r})\boldsymbol{P}_{\rm s}^{\perp}\boldsymbol{x}\right\|_2^2}{\left\|\boldsymbol{P}_{\rm s}^{\perp}\boldsymbol{g}(\boldsymbol{\Phi},\boldsymbol{r})\right\|_2^2\sigma^2/2},\tag{9}$$

where $\boldsymbol{r}=[x,y,z]$ is the potential target position and $\boldsymbol{R}^{1\times3}$ is the range of the potential target positions; $\boldsymbol{P}_{\rm s}^{\perp}=\boldsymbol{I}_N-\boldsymbol{g}(\boldsymbol{\Phi},\boldsymbol{r}_{\rm s})\boldsymbol{g}^{\rm H}(\boldsymbol{\Phi},\boldsymbol{r}_{\rm s})/\left\|\boldsymbol{g}(\boldsymbol{\Phi},\boldsymbol{r}_{\rm s})\right\|_2^2$ is the orthogonal projection

matrix onto the subspace $\langle \boldsymbol{g}(\boldsymbol{\Phi}, \boldsymbol{r}_s)\rangle^{\perp}$ that is perpendicular to the direct blast subspace $\langle \boldsymbol{g}(\boldsymbol{\Phi}, \boldsymbol{r}_s)\rangle$. This detector essentially matches the received data with the projected components of the signal wavefronts for different target positions in the orthogonal complement subspace of the direct blast subspace, effectively achieving the detection task.

However, the shallow-water environment exhibits significant environmental uncertainties. It is difficult to accurately obtain all environmental parameters; we usually only know their limits (e.g., the water depth is within 102.5 ± 2.5 m), which may lead to environmental mismatch and degrade detection performance. Figure 2 shows a typical uncertain shallow-water environment, which is referred to as the "GENLMIS" waveguide and was used in the May 1993 NRL workshop.[28] The typical uncertain environmental parameters considered in this paper, along with their limits, are given in Table 1, which can form an uncertainty set of environmental parameters as

$$\begin{aligned} \boldsymbol{R}_{\Phi} = \Big\{ & \boldsymbol{\Phi} | D_1 \in [100\ \text{m}, 105\ \text{m}],\ D_2 = 100\ \text{m}, \ldots, \\ & \alpha \in [0.1\ \text{dB}/\lambda, 0.6\ \text{dB}/\lambda] \Big\}, \end{aligned} \tag{10}$$

where the environmental parameters vector $\boldsymbol{\Phi} = [D_1, D_2, \ldots, \alpha]$, including all the parameters considered in Table 1, represents a realization of the "GENLMIS" waveguide and is unknown to the detectors.

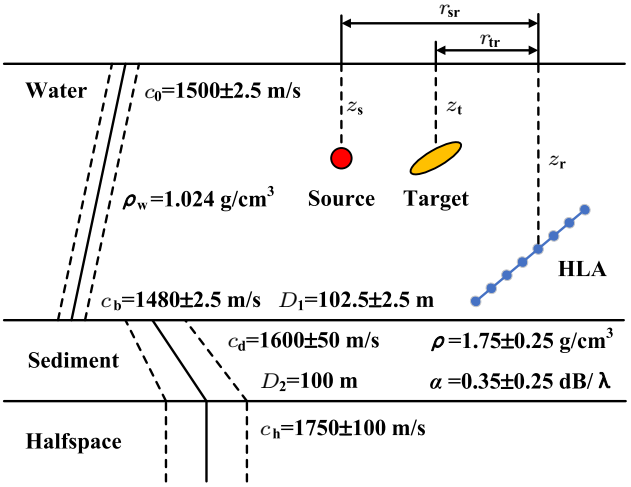


Fig. 2. Environmental configuration of the GENLMIS model (the solid line and the dashed line represent the mean parameters and the ranges of parameters, respectively).

Table 1. Environmental parameters of the GENLMIS waveguide.

Environmental parameters	Symbol	Value range
Water depth	D_1	102.5 ± 2.5 m
Sediment depth	D_2	100 m
Surface sound speed	c_0	1500 ± 2.5 m/s
Bottom sound speed	c_b	1480 ± 2.5 m/s
Sediment sound speed	c_d	1600 ± 50 m/s
Halfspace sound speed	c_h	1750 ± 100 m/s
Water density	ρ_w	1.024 g/cm^3
Sediment density	ρ	1.75 ± 0.25 g/cm^3
Sediment attenuation	α	0.35 ± 0.25 dB/λ

The direct blast/signal wavefront reflects information about the environment and the source/target positions. To address the uncertainty problem, we account for environmental uncertainties and translate them to wavefront uncertainties. Utilizing the prior knowledge of the limits of environmental parameters, the uncertainty sets within which the direct blast/signal lies can be given by

$$\begin{aligned} C_{\text{source}} &= \{ \boldsymbol{g}(\boldsymbol{\Phi}, \boldsymbol{r}_s) | \boldsymbol{\Phi} \in R_{\Phi}, \boldsymbol{r}_s = [x_s, y_s, z_s] \}, \\ C_{\text{target}} &= \left\{ \boldsymbol{g}(\boldsymbol{\Phi}, \boldsymbol{r}_t) | \boldsymbol{\Phi} \in R_{\Phi}, x_t \in R_x, y_t \in R_y, z_t \in R_z \right\}, \end{aligned} \tag{11}$$

where $\boldsymbol{r}_s = [x_s, y_s, z_s]$ is the prior known source position and $\boldsymbol{r}_t = [x_t, y_t, z_t]$ is the potential target position with the limits of R_x, R_y, R_z, which is the only difference between these two uncertainty sets.

The detection problem under uncertain environmental parameters has been transformed into a detection problem under uncertain wavefronts. Utilizing the difference between the uncertainty sets of the direct blast wavefront and the signal wavefront, it is possible to detect a target in the presence of direct blast in uncertain shallow-water environments.

3. Generalized likelihood ratio detector for forward scattering detection

3.1. GLRD

The GLRD is commonly used to address uncertainty problems by replacing all unknown parameters with their maximum likelihood estimates (MLEs). In the forward scattering detection scenario, as described in Eq. (8), the probability density functions of the data $\boldsymbol{x}$ under two hypotheses can be given by[19,23]

$$\begin{aligned} p(\boldsymbol{x}|\mathcal{H}_0; \hat{a}) &= \left(\frac{1}{\pi\sigma^2}\right)^N \exp\left(-\frac{\|\boldsymbol{x} - \boldsymbol{g}(\boldsymbol{\Phi}, \boldsymbol{r}_s)\hat{a}\|_2^2}{\sigma^2}\right), \\ p(\boldsymbol{x}|\mathcal{H}_1; \hat{a}, \hat{b}) &= \left(\frac{1}{\pi\sigma^2}\right)^N \\ &\quad \times \exp\left(-\frac{\left\|\boldsymbol{x} - \boldsymbol{g}(\boldsymbol{\Phi}, \boldsymbol{r}_s)\hat{a} - \boldsymbol{g}(\boldsymbol{\Phi}, \boldsymbol{r}_t)\hat{b}\right\|_2^2}{\sigma^2}\right), \end{aligned} \tag{12}$$

where $\hat{a}|\mathcal{H}_0 = \left(\boldsymbol{g}^{\text{H}}(\boldsymbol{\Phi}, \boldsymbol{r}_s)\boldsymbol{g}(\boldsymbol{\Phi}, \boldsymbol{r}_s)\right)^{-1}\boldsymbol{g}^{\text{H}}(\boldsymbol{\Phi}, \boldsymbol{r}_s)\boldsymbol{x}$, which is the MLE of a in null hypothesis; $\left[\hat{a}, \hat{b}\right]^{\text{T}}|\mathcal{H}_1 = \left(\boldsymbol{G}^{\text{H}}\boldsymbol{G}\right)^{-1}\boldsymbol{G}^{\text{H}}\boldsymbol{x}$, which are the MLEs of a, b in alternative hypothesis, where $\boldsymbol{G} = [\boldsymbol{g}(\boldsymbol{\Phi}, \boldsymbol{r}_s), \boldsymbol{g}(\boldsymbol{\Phi}, \boldsymbol{r}_t)]$; $\|\cdot\|_2$ is the two-norm. Due to environmental uncertainties, the direct blast wavefront and the signal wavefront are unknown, and their MLEs are denoted by

$$\begin{aligned} \hat{\boldsymbol{g}}(\boldsymbol{\Phi}, \boldsymbol{r}_s)|\mathcal{H}_0 &= \arg\max_{C_{\text{source}}} p(\boldsymbol{x}|\mathcal{H}_0; \hat{a}, \tilde{\boldsymbol{g}}), \\ \hat{\boldsymbol{G}}|\mathcal{H}_1 &= \arg\max_{C} p\left(\boldsymbol{x}|\mathcal{H}_1; \hat{a}, \hat{b}, \tilde{\boldsymbol{G}}\right), \end{aligned} \tag{13}$$

where $C=\left[\boldsymbol{G}|\boldsymbol{g}\left(\boldsymbol{\Phi},\boldsymbol{r}_{\mathrm{s}}\right)\in C_{\mathrm{source}},\boldsymbol{g}\left(\boldsymbol{\Phi},\boldsymbol{r}_{\mathrm{t}}\right)\in C_{\mathrm{target}}\right]$ is the uncertainty set of $\boldsymbol{G}$; $\tilde{\boldsymbol{g}}$ and $\tilde{\boldsymbol{G}}$ are an arbitrary vector in uncertainty set C_{source} and an arbitrary matrix in uncertainty set C, respectively.

The generalized likelihood ratio can be given by

$$L\left(\boldsymbol{x}\right)=\frac{\max\limits_{C}p\left(\boldsymbol{x}|\mathcal{H}_1;\hat{a},\hat{b},\tilde{\boldsymbol{G}}\right)}{\max\limits_{C_{\mathrm{source}}}p\left(\boldsymbol{x}|\mathcal{H}_0;\hat{a},\tilde{\boldsymbol{g}}\right)},\tag{14}$$

whose logarithmic form is used as the test statistic that is

$$T\left(\boldsymbol{x}\right)=2\ln L\left(\boldsymbol{x}\right)=\max_{C}\frac{\boldsymbol{x}^{\mathrm{H}}\boldsymbol{P}_G\boldsymbol{x}}{\sigma^2/2}-\max_{C_{\mathrm{source}}}\frac{\boldsymbol{x}^{\mathrm{H}}\boldsymbol{P}_g\boldsymbol{x}}{\sigma^2/2},\tag{15}$$

where $\boldsymbol{P}_G=\tilde{\boldsymbol{G}}\left(\tilde{\boldsymbol{G}}^{\mathrm{H}}\tilde{\boldsymbol{G}}\right)^{-1}\tilde{\boldsymbol{G}}^{\mathrm{H}}$ and $\boldsymbol{P}_g=\tilde{\boldsymbol{g}}\left(\tilde{\boldsymbol{g}}^{\mathrm{H}}\tilde{\boldsymbol{g}}\right)^{-1}\tilde{\boldsymbol{g}}^{\mathrm{H}}$ are the orthogonal projection matrices onto the subspace $\langle\tilde{\boldsymbol{G}}\rangle$ and the subspace $\langle\tilde{\boldsymbol{g}}\rangle$, respectively. In fact, the former in Eq. (15) is the best match of the direct blast wavefront and the signal wavefront to achieve the maximum processing gain, and the latter is just the best match of the direct blast wavefront, which can be effectively suppressed through subtraction. Subsequently, the remaining signal energy after direct blast suppression is used for detection.

3.2. Performance measure

The performance measure of the GLRD for forward scattering detection is difficult to obtain directly from the distribution of $T\left(\boldsymbol{x}\right)$ in Eq. (15), since the distributions under two hypotheses cannot be derived theoretically when both the environmental parameters and the target position are unknown. Alternatively, we derive the deflection coefficient[29] to approximately characterize its performance, which is the ratio of the difference in mean of the test statistic T under $\mathcal{H}_0$ and $\mathcal{H}_1$ to the standard deviation of T under $\mathcal{H}_0$ and is denoted by

$$\kappa=\frac{E\left(T|\mathcal{H}_1\right)-E\left(T|\mathcal{H}_0\right)}{\sqrt{D\left(T|\mathcal{H}_0\right)}},\tag{16}$$

where $E\left(\cdot\right)$ and $D\left(\cdot\right)$ denote the mean and the variance respectively. To derive an analytical expression for Eq. (16), we make the following two assumptions.

Assumption 1 The MLEs of $\boldsymbol{G}$ and $\boldsymbol{g}\left(\boldsymbol{\Phi},\boldsymbol{r}_{\mathrm{s}}\right)$ are independent of the noise and only determined by the direct blast and the signal. This is reasonable when the energy of these signals is much higher than that of the noise.

Assumption 2 The uncertainty sets of the direct blast wavefront and signal wavefront are large enough. In other words, the real wavefronts of them are sampled within these uncertainty sets.

Under the assumption 1, the MLEs of $\boldsymbol{G}$ and $\boldsymbol{g}\left(\boldsymbol{\Phi},\boldsymbol{r}_{\mathrm{s}}\right)$ in the null hypothesis $\mathcal{H}_0$ and in the alternative hypothesis $\mathcal{H}_1$ can be denoted by

$$\begin{aligned}
&\hat{\boldsymbol{G}}_0=\hat{\boldsymbol{G}}|\mathcal{H}_0=\arg\max_{C}\left\|\boldsymbol{P}_G\boldsymbol{s}_{\mathrm{source}}\right\|_2^2,\\
&\hat{\boldsymbol{G}}_1=\hat{\boldsymbol{G}}|\mathcal{H}_1=\arg\max_{C}\left\|\boldsymbol{P}_G\left(\boldsymbol{s}_{\mathrm{source}}+\boldsymbol{s}_{\mathrm{target}}\right)\right\|_2^2,\\
&\hat{\boldsymbol{g}}_0=\hat{\boldsymbol{g}}\left(\boldsymbol{\Phi},\boldsymbol{r}_{\mathrm{s}}\right)|\mathcal{H}_0=\arg\max_{C_{\mathrm{source}}}\left\|\boldsymbol{P}_g\boldsymbol{s}_{\mathrm{source}}\right\|_2^2,\\
&\hat{\boldsymbol{g}}_1=\hat{\boldsymbol{g}}\left(\boldsymbol{\Phi},\boldsymbol{r}_{\mathrm{s}}\right)|\mathcal{H}_1=\arg\max_{C_{\mathrm{source}}}\left\|\boldsymbol{P}_g\left(\boldsymbol{s}_{\mathrm{source}}+\boldsymbol{s}_{\mathrm{target}}\right)\right\|_2^2.
\end{aligned}\tag{17}$$

Meanwhile, we rewrite the test statistic T as a quadratic form as

$$T\left(\boldsymbol{x}\right)=\frac{\boldsymbol{x}^{\mathrm{H}}\boldsymbol{A}\boldsymbol{x}}{\sigma^2/2},\tag{18}$$

where $\boldsymbol{A}=\boldsymbol{P}_{\hat{G}}-\boldsymbol{P}_{\hat{g}}$ is an $N\times N$ Hermitian matrix; $\boldsymbol{P}_{\hat{G}}=\hat{\boldsymbol{G}}\left(\hat{\boldsymbol{G}}^{\mathrm{H}}\hat{\boldsymbol{G}}\right)^{-1}\hat{\boldsymbol{G}}^{\mathrm{H}}$ and $\boldsymbol{P}_{\hat{g}}=\hat{\boldsymbol{g}}\left(\hat{\boldsymbol{g}}^{\mathrm{H}}\hat{\boldsymbol{g}}\right)^{-1}\hat{\boldsymbol{g}}^{\mathrm{H}}$ are the orthogonal projection matrices onto the subspaces spanned by the MLEs of $\boldsymbol{G}$ and $\boldsymbol{g}\left(\boldsymbol{\Phi},\boldsymbol{r}_{\mathrm{s}}\right)$, respectively.

The deflection coefficient of this quadratic test statistic can be denoted by (the derivation processes are shown in Appendix A)

$$\kappa=\frac{\mathrm{tr}\left(\boldsymbol{A}_1\boldsymbol{R}\right)-\mathrm{tr}\left(\boldsymbol{A}_0\boldsymbol{R}_{\mathrm{source}}\right)}{\sqrt{\sigma^4\mathrm{tr}\left(\boldsymbol{A}_0^2\right)+2\sigma^2\left\|\boldsymbol{A}_0\boldsymbol{s}_{\mathrm{source}}\right\|_2^2}},\tag{19}$$

where

$$\begin{aligned}
&\boldsymbol{R}_{\mathrm{source}}=E\left(\boldsymbol{s}_{\mathrm{source}}\boldsymbol{s}_{\mathrm{source}}^{\mathrm{H}}\right),\\
&\boldsymbol{R}=E\left[\left(\boldsymbol{s}_{\mathrm{source}}+\boldsymbol{s}_{\mathrm{target}}\right)\left(\boldsymbol{s}_{\mathrm{source}}+\boldsymbol{s}_{\mathrm{target}}\right)^{\mathrm{H}}\right]
\end{aligned}$$

are the spatial covariance matrices of the signal under $\mathcal{H}_0$ and $\mathcal{H}_1$, respectively; $\boldsymbol{A}_i=\boldsymbol{P}_{\hat{G}_i}-\boldsymbol{P}_{\hat{g}_i}$, $i=0,1$.

The performance of the GLRD is approximately measured by Eq. (19), but it is still difficult to analyze the detection performance since the MLEs of $\boldsymbol{G}$ and $\boldsymbol{g}\left(\boldsymbol{\Phi},\boldsymbol{r}_{\mathrm{s}}\right)$ cannot be expressed analytically. Therefore, based on Assumption 1, we also take Assumption 2 into account to derive an expression for quantifying the performance of the GLRD. Under these two assumptions, the deflection coefficient can be rewritten as (the derivation processes are shown in Appendix B)

$$\begin{aligned}
\kappa&=\frac{\left\|\boldsymbol{s}_{\mathrm{source}}+\boldsymbol{s}_{\mathrm{target}}\right\|_2^2-\max\limits_{C_{\mathrm{source}}}\left\|\boldsymbol{P}_g\left(\boldsymbol{s}_{\mathrm{source}}+\boldsymbol{s}_{\mathrm{target}}\right)\right\|_2^2}{\sigma^2}\\
&\leq\frac{\left(1-|\gamma|^2\right)\left\|\boldsymbol{s}_{\mathrm{target}}\right\|_2^2}{\sigma^2}=\kappa_{\mathrm{opt}},
\end{aligned}\tag{20}$$

where $\gamma=\frac{\boldsymbol{s}_{\mathrm{source}}^{\mathrm{H}}\boldsymbol{s}_{\mathrm{target}}}{\left\|\boldsymbol{s}_{\mathrm{source}}\right\|_2\left\|\boldsymbol{s}_{\mathrm{target}}\right\|_2}$ represents the correlation between the direct blast and the signal. When $\hat{\boldsymbol{g}}_1=\boldsymbol{g}\left(\boldsymbol{\Phi},\boldsymbol{r}_{\mathrm{s}}\right)$, the deflection coefficient reaches its maximum value. In Eq. (20), the first term, $\left\|\boldsymbol{s}_{\mathrm{source}}+\boldsymbol{s}_{\mathrm{target}}\right\|_2^2$, represents the total energy of the received data, including forward scattering signal and the direct blast. The second term, $\max\limits_{C_{\mathrm{source}}}\left\|\boldsymbol{P}_g\left(\boldsymbol{s}_{\mathrm{source}}+\boldsymbol{s}_{\mathrm{target}}\right)\right\|_2^2$, represents the energy of the received data projected onto the subspace $\langle\hat{\boldsymbol{g}}_1\rangle$, which is regarded as direct blast energy and is thus suppressed.

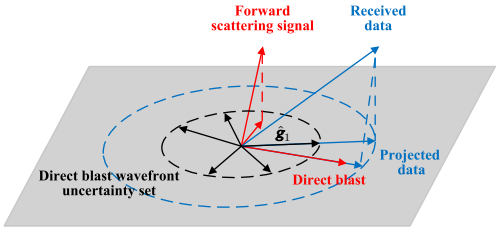


Fig. 3. Schematic of projection under $\mathcal{H}_1$.

Although the forward scattering signal is highly correlated with the direct blast, its projection in the subspace defined by the direct blast wavefront is not always maximized; that is, its projection may deviate from the direct blast wavefront, as shown in Fig. 3. This results in the MLE of the direct blast wavefront under hypothesis $\mathcal{H}_1$ deviating from the true value, and leads to an increase in the energy of the received data projected into the subspace $\langle\hat{\boldsymbol{g}}_1\rangle$. Consequently, the suppressed energy exceeds that of the direct blast itself, leading to performance degradation.

When the signal is uncorrelated with the wavefronts in the direct blast wavefront uncertainty set, or the intensity of the direct blast is much higher than that of the signal (i.e., low signal-to-direct blast ratio, SDR), the signal energy projected into subspace $\langle\hat{\boldsymbol{g}}_1\rangle$ can be rejected, as it contributes little to the estimation of the direct blast wavefront. In such case, $\hat{\boldsymbol{g}}_1 = \hat{\boldsymbol{g}}(\boldsymbol{\Phi}, \boldsymbol{r}_s)\,|\mathcal{H}_1 \approx \boldsymbol{g}(\boldsymbol{\Phi}, \boldsymbol{r}_s)$, and the GLRD can reach its optimal performance κ_{opt}, which is only determined by the signal-to-noise ratio (SNR) and the correlation between the direct blast and the signal.

4. Simulations and results

In this section, we analyze the performance of the GLRD with forward scattering, focusing on both its theoretical and real performance through simulations conducted in the GENLMIS waveguide. The theoretical performance is characterized by the detection capabilities of the GLRD, with uncertainty sets that are sufficiently large to encompass both the real direct blast wavefront and the real signal wavefront. Similarly, the real performance is characterized by the detection capabilities of the GLRD, with sampling uncertainty sets constituted by wavefronts obtained through Monte Carlo sampling across the entire uncertainty set, i.e., the sampling uncertainty sets are part of the entire uncertainty set and may not encompass the real wavefronts. To distinguish between these two scenarios, we refer to the former as the optimal generalized likelihood ratio detector (Opt-GLRD) and the latter as the generalized likelihood ratio detector based on Monte Carlo optimization (MC-GLRD).

First, we analyze the impact of the source direction relative to the HLA and the array aperture on the performance of the GLRD. Based on these simulation results, the subsequent simulations are conducted with a 1000-element HLA, maintaining the source positioned on the broadside of the array. Secondly, the influences of signal-to-noise ratio (SNR) and signal-to-direct blast ratio (SDR) on detection performance are simulated, where $\text{SNR} = \left\|\boldsymbol{s}_{\text{target}}\right\|_2^2/\sigma^2$ and $\text{SDR} = \left\|\boldsymbol{s}_{\text{target}}\right\|_2^2/\left\|\boldsymbol{s}_{\text{source}}\right\|_2^2$, and the robustness of the GLRD to environmental uncertainties is explored by investigating its performance across different environment scenarios. Finally, we compare the performance of the GLRD in the forward scattering detection with that in the backward scattering detection, and the results demonstrate that the former performs better than the latter.

The simulation conditions are shown in Figs. 1 and 2. A source is located at $\boldsymbol{r}_s = [10\,\text{km}, 0]$ and transmits the signal with the frequency of 1 kHz at the depth of $z_s = 50$ m. An N-element HLA is mounted on the bottom (i.e., $z_r = D_1$) with the element spacing of $d = 0.75$ m. The center of the HLA is located at [0,0] and the nth element is located at

$$\boldsymbol{r}_{r_n} = \left[\frac{-N-1+2n}{2}d\cos\varphi_{\text{array}}, \frac{-N-1+2n}{2}d\sin\varphi_{\text{array}}\right], \quad n = 1, 2, \ldots, N, \tag{21}$$

where φ_{array} is the angle between the HLA and the x-axis. Two special cases should be noted. When $\varphi_{\text{array}} = \pi/2$, the HLA is perpendicular to the x-axis, meaning the source is positioned on the broadside of the HLA. When $\varphi_{\text{array}} = 0$, the HLA is parallel to the x-axis, meaning the source is positioned in the end-fire direction of the HLA.

Moreover, we use a rigid prolate spheroid[30] with a semi-major axis of 7.5 m and a semi-minor axis of 1 m as the underwater target, and its scattering function is denoted as $S_r(\theta, \varphi; \theta_0, \varphi_0)$. Considering that the SDR is fixed in a given detection scenario, we use a constant D to control the magnitude of the TS, which does not alter its spatial distribution but allows us to analyze the detector performance in a specific SDR detection scenario. In other words, the scattering function used in the simulations is denoted

$$S(\theta, \varphi; \theta_0, \varphi_0) = DS_r(\theta, \varphi; \theta_0, \varphi_0). \tag{22}$$

Two hundred positions are uniformly sampled from the potential target positions in xOz plane. For each sampled position, 50 environments are randomly sampled in the GENLMIS waveguide, and the associated direct blast/signal wavefronts are calculated. Therefore, 10000 direct blast/signal wavefronts are sampled in uncertainty sets C_{source} and C_{target} for the MC-GLRD. All simulations were conducted with 10000 independent trials to calculate the detection probability P_d with a false alarm probability $P_{fa} = 0.01$.

4.1. Forward scattering detection configuration

The configuration of the forward scattering detection, specifically the source azimuth angle and array aperture, significantly affects detection performance. Figure 4(a) shows the

maximum correlation between the real direct blast wavefront and the sampled direct blast wavefronts, as well as between the real signal wavefront and the sampled signal wavefronts, for different source azimuth angles when the target is positioned at $\boldsymbol{r}_{\rm t} = [5\ {\rm km}, 0, 50\ {\rm m}]$ in the GENLMIS waveguide with mean parameters as shown in Table 2. This mean environmental parameters condition is a realization of the GENLMIS waveguide and is unknown to the detectors. Both correlations reach their maximum values when the source is positioned on the broadside of the HLA. Consequently, the HLA demonstrates robustness to environmental mismatches in this direction, resulting in optimal detection performance for the MC-GLRD, as shown in Fig. 4(b).

Although the Opt-GLRD always works well for all source azimuth angles in the forward scattering detection, the MC-GLRD can only work when the source is positioned around the broadside. Considering that we cannot always accurately obtain the real wavefronts in reality, the performance of the Opt-GLRD may not always be achievable, and the MC-GLRD exhibits more common detection performance. Therefore, we set $\varphi_{\rm array} = 90^\circ$ in subsequent simulations.

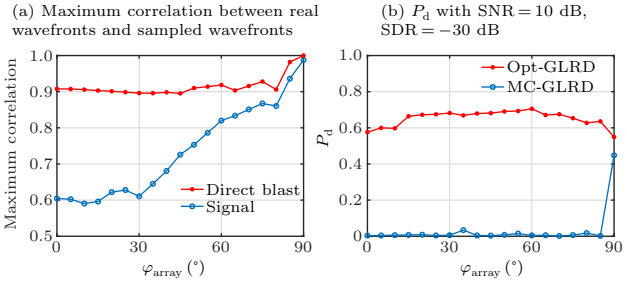


Fig. 4. Performance of the GLRD under different $\varphi_{\rm array}$ conditions in the GENLMIS waveguide with mean parameters, when the element number $N = 1000$ and frequency $f = 1000$ Hz.

Table 2. The mean environmental parameters.

Parameters	D_1 (m)	D_2 (m)	c_0 (m/s)	$c_{\rm b}$ (m/s)	$c_{\rm d}$ (m/s)	$c_{\rm h}$ (m/s)	$\rho_{\rm w}$ (g/cm^3)	ρ (g/cm^3)	α (dB/λ)
Values	102.5	100	1500	1480	1600	1750	1.024	1.75	0.35

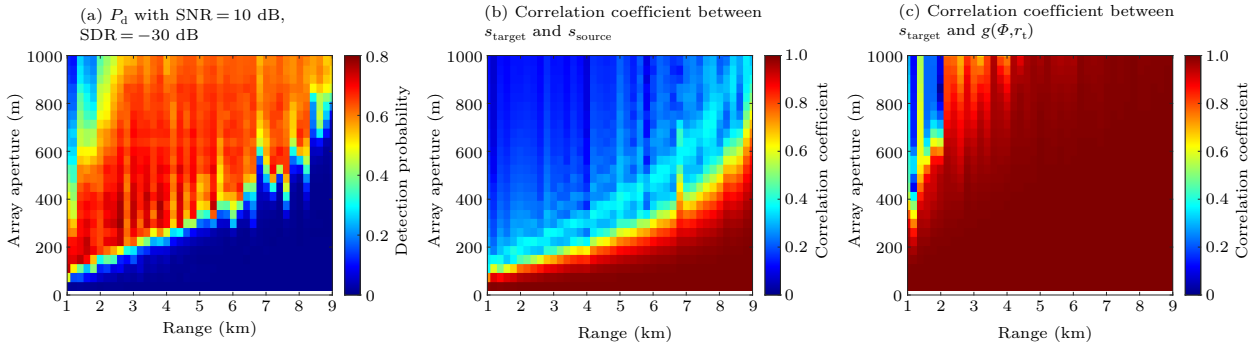


Fig. 5. Performance of the GLRD under different array aperture conditions in the GENLMIS waveguide with the mean parameters, when the source azimuth angle $\varphi_{\rm array} = 90^\circ$ and frequency $f = 1000$ Hz.

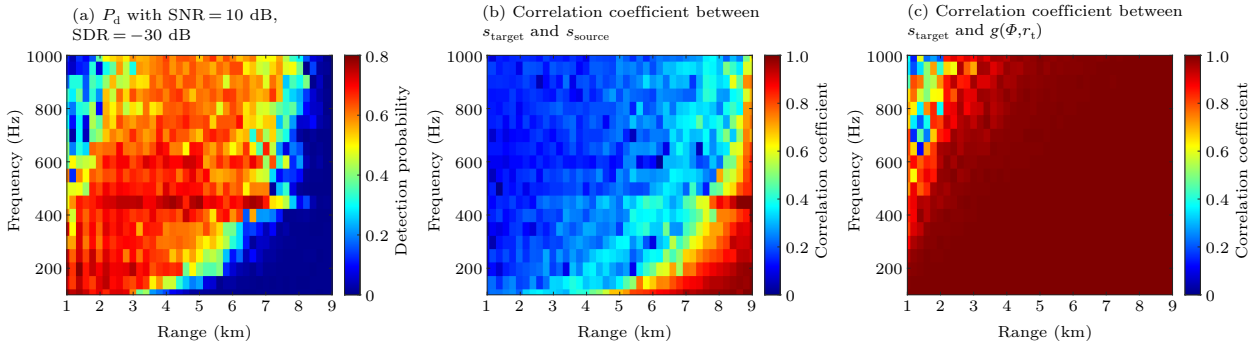


Fig. 6. Performance of the GLRD under different frequency conditions in the GENLMIS waveguide with the mean parameters, when the source azimuth angle $\varphi_{\rm array} = 90^\circ$ and the element number $N = 1000$.

Forward scattering detection depends on the difference between the direct blast and the signal. It is very difficult to detect a target using a short array under low-frequency conditions, because the direct blast and the signal are so similar that both are suppressed. Figures 5 and 6 respectively show the performance of the Opt-GLRD under different array aperture and frequency conditions in the GENLMIS waveguide with mean parameters when the target is at a depth of $z_{\rm t} = 50$ m. With the increase of the array aperture and frequency, the correlation between the direct blast and the signal decreases, resulting in an increase of the remaining signal energy after direct blast suppression, so the detection performance is improved.

However, we notice that the performance degrades in the near field with a large aperture and high frequency. This degradation results from the mismatch between the real signal and

the approximate signal. Specifically, under high-frequency conditions, the forward scattering main lobe is very narrow, and not all elements of the large aperture array can be located within the scattering main lobe. The assumption in Eq. (5), which approximates the TS as equal in the direction from φ_1 to φ_N, no longer holds, and the directivity of target scattering in space cannot be ignored anymore. In contrast, under low-frequency conditions, the forward scattering main lobe is wide, and all elements of the small aperture array are located within the scattering main lobe. The assumption holds, and the GLRD exhibits good performance in the near field. Considering the detection performance in both the near-field and far-field, we use the number of elements $N = 1000$ and the frequency $f = 1000$ Hz in subsequent simulations.

4.2. Performance analysis

Many factors affect the detector performance. In this section, we mainly analyze the effects of the environment, SNR, and SDR on the detector performance.

According to Eq. (20), the deflection coefficient, which characterizes the detection performance, is weakly dependent on the environments. Therefore, the GLRD may exhibit similar performance across different environmental scenarios when the uncertainty sets of wavefronts are large enough. Figure 7 shows the detection probability of the GLRD across 100 random environmental realizations, with the target positioned at $\boldsymbol{r}_t = [5\ \text{km}, 0, 50\ \text{m}]$. Although the Opt-GLRD exhibits performance fluctuations across different environments due to the varying correlations between the direct blast and the signal, it still maintains a certain degree of robustness against environmental uncertainties, as analyzed above. Similarly, the performance of the MC-GLRD is affected not only by these correlations but also by the limited number of sampled wavefronts. These limited sampled wavefronts exhibit varying correlations with the real wavefronts across different environments, further affecting the performance and resulting in insufficient robustness against environmental uncertainties

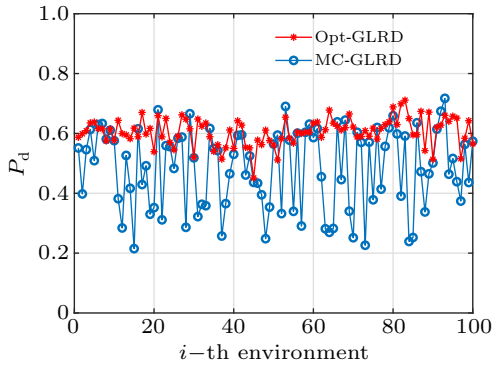


Fig. 7. Performance of the GLRD under 100 random environmental realizations with SNR = 10 dB and SDR = −30 dB.

Direct blast is the main issue in the forward scattering detection problem. By suppressing the intense direct blast, the remaining signal energy is used for detection and the target can be detected. Figure 8(a) shows the performance of the GLRD under different SDR conditions, with the target positioned at $\boldsymbol{r}_t = [5\ \text{km}, 0, 50\ \text{m}]$. As analyzed in Subsection 3.2, with low SDRs, the MLE of the direct blast wavefront under hypothesis $\mathcal{H}_1$ can be closer to its true value, allowing for complete suppression of the direct blast while the signal energy is almost entirely preserved. Therefore, the Opt-GLRD can reach its optimal performance κ_{opt} and presents good resistance against the direct blast. On the contrary, since the real wavefronts do not lie in the sampling uncertainty sets, the direct blast cannot be completely suppressed for the MC-GLRD. Consequently, the residual direct blast energy after suppression remains significant under low SDR conditions, leading to the failure of the MC-GLRD.

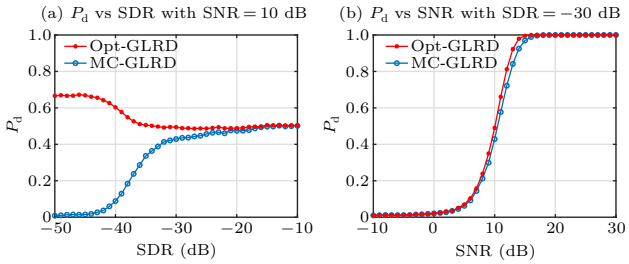


Fig. 8. Performance of the GLRD under different (a) SDR and (b) SNR conditions in the GENLMIS waveguide with the mean parameters.

Moreover, although the MLE of the direct blast wavefront under hypothesis $\mathcal{H}_1$ deviates from the true value under high SDR conditions, the residual direct blast energy after suppression is small due to the reduced intensity of the direct blast. As a result, both the Opt-GLRD and the MC-GLRD exhibit good performance with high SDRs.

4.3. Compared to the backward scattering detection

Although the intensity of the scattered signal in the forward direction is much higher than in the backward direction, forward scattering detection faces the additional challenge of intense direct blast, which does not exist in backward scattering detection. Therefore, the relative performance of the GLRD in these two detection scenarios requires further investigation, which we will conduct in this section.

We consider such a realistic detection scenario where the underwater target, a rigid prolate spheroid with a semi-major axis of 7.5 m and a semi-minor axis of 1 m (i.e., $D = 1$), crosses the baseline connecting the source and the receiver when $\boldsymbol{r}_t = [5\ \text{km}, 0, 50\ \text{m}]$. In this case, the SDR = −35.87 dB, and the performance of the GLRD in forward and backward scattering detection is shown in Fig. 9, with an ambient noise level (NL) of 90 dB. Compared to backward scattering, the SNR in forward scattering improves by approximately 10 dB. Therefore, even the MC-GLRD in forward scattering detection outperforms the Opt-GLRD in backward scattering detection.

However, this conclusion is not always valid. Many factors can affect target strength, such as frequency, which may lead to variations in performance between forward scattering detection and backward scattering detection. Figure 10 shows the performance of the GLRD under different frequency conditions. Since the target strength in backward scattering is higher than that in forward scattering under low-frequency conditions, the backward scattering signal exhibits a higher SNR than the forward scattering signal. As a result, the detection performance of the former exceeds that of the latter.

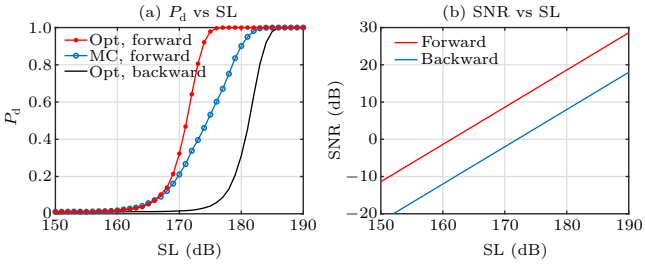


Fig. 9. Performance of the GLRD in forward and backward scattering detections in the GENLMIS waveguide with the mean parameters, and NL = 90 dB, SDR = −35.87 dB.

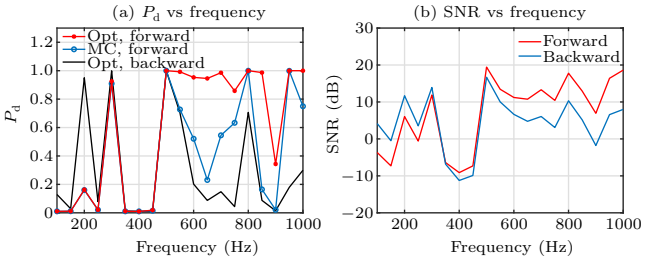


Fig. 10. Performance of the GLRD in forward and backward scattering detections under different frequency conditions, and NL = 90 dB, SL = 180 dB.

Additionally, under high-frequency conditions, the main lobe of forward scattering is very narrow. When the target deviates from the source-receiver baseline, the receiver may fall outside the main lobe. This may cause the SNR to decrease rapidly and lead to performance degradation of the detectors. Considering that the potential target position extends from the source-receiver baseline to the vicinity of this line, the uncertainty of the target position increases. Therefore, we increase the number of sampled wavefronts from 10000 to 50000 to enhance the effectiveness of MC-GLRD in detecting a target that deviates from the baseline.

Figure 11 shows the performance of the GLRD when the target is at $\boldsymbol{r}_t = [5\text{ km}, y, 50\text{ m}]$, where y is the distance that the target deviates from the baseline. With a narrow main lobe of forward scattering, the performance of forward scattering detection begins to decrease when this distance exceeds 200 m, which is less than the distance in backward scattering detection. The distance of 200 m here applies only to this specific simulation condition; it varies from case to case and depends on target sizes, frequencies, and other factors. Generally, as target size and frequency increase, the forward scattering main lobe becomes narrower.[31] Therefore, the allowable deviation distance from the source-receiver baseline also decreases.

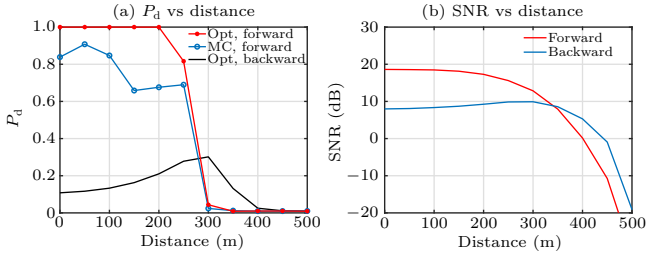


Fig. 11. The performance of the GLRD in forward and backward scattering detections when the target deviates from the source-receiver baseline at different distances, and NL = 90 dB, SL = 180 dB.

5. Experimental data results

In this section, we use the data from the SWellEx-96 experiment, which was conducted in May 1996, approximately 12 km from the tip of Point Loma near San Diego, California, to evaluate the performance of the GLRD. Figure 12 shows the source ship track during independent events S5 and S59 in the experiment. The ship proceeded northward at 5 knots (2.5 m/s), with square markers indicating its position every 5 min. Fifty-one CTD surveys were conducted during the entire experiment to provide water column sound speed data, and detailed environmental parameters are given in Fig. 13 according to data from CTD #20.

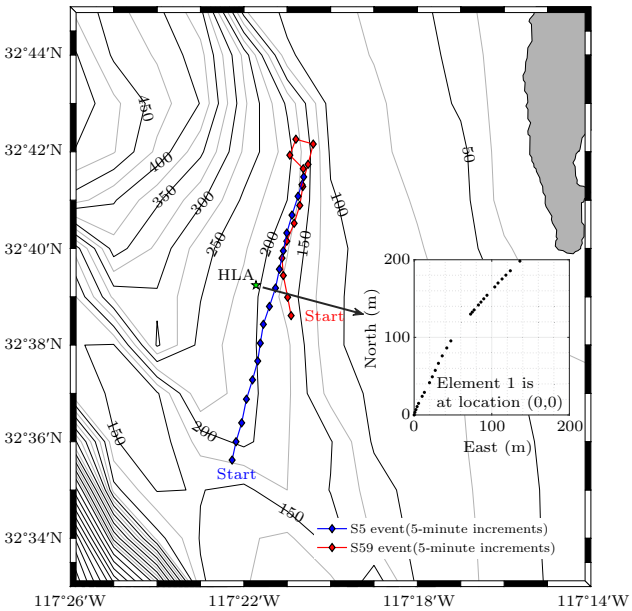


Fig. 12. Map of the source track in event S5 (blue color) and event S59 (red color).

An HLA, consisting of 27 available elements, is deployed on the seafloor, and sampled data with sampling rate 3276.8 Hz. The HLA received the last 50 min of the data (9830400 points) during the event S5 which totally lasted for 75 min, and the full 65 min of the data (12779521 points) during the event S59. We divided the date with 1.25 s snapshot length (4096 points) as a segment, with 50% (2048 points) overlap between successive snapshots, and transformed them

to the frequency domain. Therefore, 4799 and 6239 frequency domain snapshots are obtained during events S5 and S59, respectively.

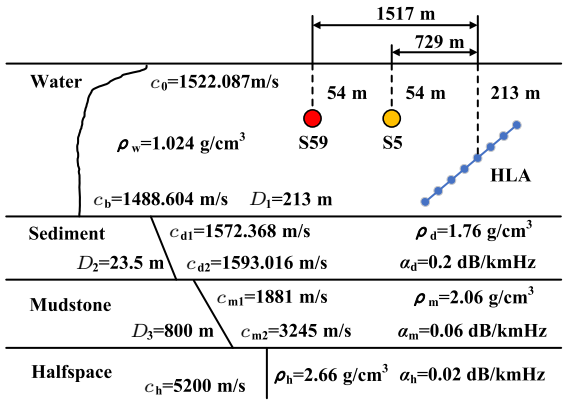


Fig. 13. Environmental configuration of SWellEx-96 experiment.

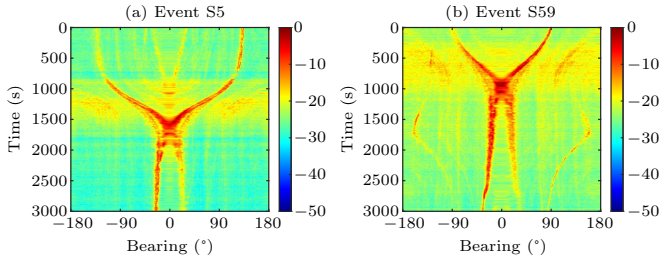


Fig. 14. Bearing estimation of MVDR.

Due to a slight bow ($\sim$ 13 m) in the entire array, we only used half of it (from the 15th to the 27th element), which is relatively straight. We processed the data at 388 Hz frequency, and the bearing estimation results of the source by minimum variance distortionless response (MVDR) during events S5 and S59 are given in Fig. 14.

According to simulation results, the GLRD performs well when both the source and the target are on the broadside of the HLA. Therefore, we selected the 388 Hz data from event S5 around the 1065th second (the 1705th frequency domain snapshot) as the signal and the 388 Hz data from the beginning of event S59 (the 24th frequency domain snapshot) as the direct blast, based on the bearing estimation results. However, the events S5 and S59 were not conducted simultaneously, and no noise-only data existed at any time in the 388 Hz frequency. We constructed synthetic data, where the 401 Hz data from event S59 is used as the noise (the real frequency is 400.8 Hz, with a frequency resolution of 0.8 Hz), and the detection problem is formulated as

$$\begin{aligned}\mathcal{H}_0 &: \boldsymbol{x}_{\rm syn} = \boldsymbol{U}_{\rm w}^{\rm H}\boldsymbol{x}_{\rm S59}^{(388)}a + \boldsymbol{U}_{\rm w}^{\rm H}\boldsymbol{x}_{\rm S59}^{(401)},\\ \mathcal{H}_1 &: \boldsymbol{x}_{\rm syn} = \boldsymbol{U}_{\rm w}^{\rm H}\boldsymbol{x}_{\rm S59}^{(388)}a + \boldsymbol{U}_{\rm w}^{\rm H}\boldsymbol{x}_{\rm S5}^{(388)}b + \boldsymbol{U}_{\rm w}^{\rm H}\boldsymbol{x}_{\rm S59}^{(401)},\end{aligned} \tag{23}$$

where $\boldsymbol{x}_{\rm syn}$ is the frequency-domain synthetic data after pre-whitening; $\boldsymbol{x}_{\rm S59}^{(388)}$ and $\boldsymbol{x}_{\rm S5}^{(388)}$ are the 388 Hz received data from events S59 and S5, respectively; $\boldsymbol{x}_{\rm S59}^{(401)}$ is the 401 Hz received data from event S59; $\boldsymbol{U}_{\rm w}$ is whitening matrix that satisfies

$$\boldsymbol{U}_{\rm w} = \boldsymbol{U}\boldsymbol{\Lambda}^{-1/2}, \tag{24}$$

where $\boldsymbol{U}$ and $\boldsymbol{\Lambda}$ are the eigenvector matrix and eigenvalue matrix of the noise covariance matrix, respectively. Although the received data from both events contain noise, we still consider these data to be pure signals and define the SNR and SDR of the synthetic data as

$$\text{SNR} = \frac{\left\|\boldsymbol{U}_{\rm w}^{\rm H}\boldsymbol{x}_{\rm S5}^{(388)}b\right\|_2^2}{\sigma_{\rm w}^2},\quad \text{SDR} = \frac{\left\|\boldsymbol{U}_{\rm w}^{\rm H}\boldsymbol{x}_{\rm S5}^{(388)}b\right\|_2^2}{\left\|\boldsymbol{U}_{\rm w}^{\rm H}\boldsymbol{x}_{\rm S59}^{(388)}a\right\|_2^2}, \tag{25}$$

where $\sigma_{\rm w}^2$ is the noise power after pre-whitening.

In simulations, we consider a detection scenario where the source is fixed while the target is moving. However, in the experiment for event S59, the source was also moving and not fixed, which caused additional position uncertainty. Taking this into account and considering that the source position should be known *a priori*, we sampled the source position for event S59 within a narrow region of 20 m $\times$ 20 m, with the geometric center of the sampling region located 1520 m from the center of the HLA. This resulted in 121 sampling points, with a sampling interval of 2 m $\times$ 2 m. The target position should be unknown, so we sampled the source position for event S5 within a large region of 700 m$\times$200 m, with the geometric center of the sampling region located 750 m from the center of the HLA, and 396 sampling points could be obtained with the same sampling interval of 20 m$\times$20 m. The detailed sampling region is given in Fig. 15.

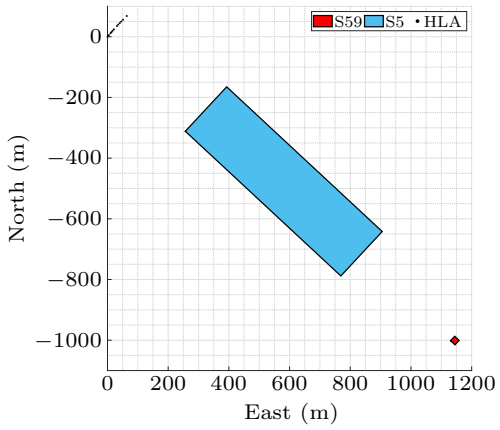


Fig. 15. Schematic of position sampling region.

Except for the position uncertainty, the environment is also uncertain. We treated each sampled source position for events S59 and S5 as a combination, and the corresponding environment was uniformly sampled based on the 51 CTD data from the experiment. Moreover, for each environment sample, we added fluctuations of $\pm$1 m/s to the water column sound speed profile and fluctuations of $\pm$1 m to the water depth. It is worth noting that the survey was conducted in different stations, most of whose water depths were less than 213 m.

Since the sound speed can be considered approximately constant at greater depth, we artificially extended the CTD data to 213 m, with the sound speed in this extended section equal to the maximum depth data from the CTD. Finally, totally 47916 sampled wavefronts were obtained.

As mentioned above, we treat the received data from events S59 and S5 at 388 Hz as pure signals, even though they still contain noise components. Moreover, due to the lack of detailed topographic data, the sampled wavefronts are computed assuming a flat seabed. These approximation processings decrease the correlation between the sampled wavefronts and the real received wavefronts, and the maximum correlation coefficients between them for events S59 and S5 are 0.8992 and 0.9542, respectively, as shown in Fig. 16. With a narrow sampling region, the correlation coefficients of the former exhibit less variation than those of the latter. However, since the source in event S59 is farther away than that in event S5, the SNR is relatively lower, resulting in this lower maximum correlation coefficient.

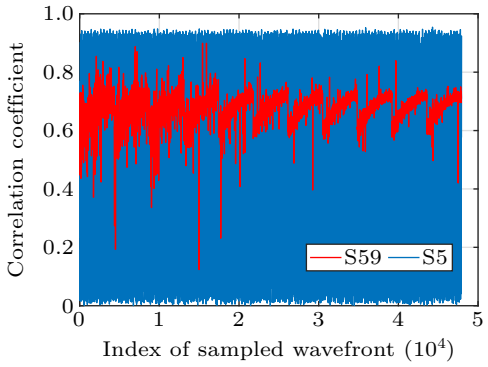


Fig. 16. Correlation between the received wavefronts and the sampled wavefronts.

These factors lead to a decrease in the direct blast suppression capability and processing gain of the GLRD. Additionally, due to the noise contained in the received data, the real SNR, whose true value is unknown, should be lower than that we preset. Figure 17 shows the performance of the GLRD under different SDR and SNR conditions with $P_{\rm fa} = 0.01$. The detection performance falls below expectations. The GLRD can work effectively with an SNR of at least 13 dB and an SDR of at most -30 dB.

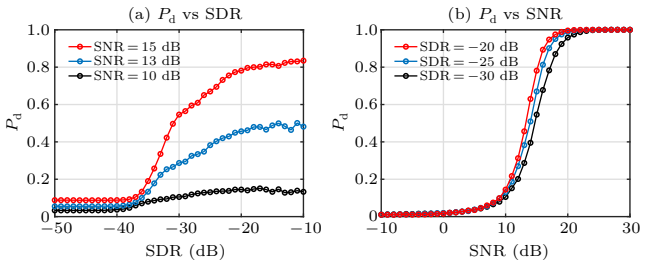


Fig. 17. Performance of the GLRD under different (a) SDR and (b) SNR conditions.

We also analyze the performance of the GLRD under different aperture conditions, where the aperture is controlled by processing only some elements of the HLA. First, we process the data from the 25th to the 27th element. Then, we incrementally include two additional elements each time, for example, processing the data from the 23rd to the 27th element, followed by the 21st to the 27th, and so on. Figure 18 shows the processing results in this case. When the aperture is insufficient, the correlation between the direct blast and the signal is so high that both are suppressed, resulting in the remaining signal energy being inadequate to support the detection task. Conversely, when the aperture is larger than 86 m, in which case the correlation between the direct blast and the signal decreases to 0.2, the GLRD can work effectively. This confirms that a large aperture HLA is necessary.

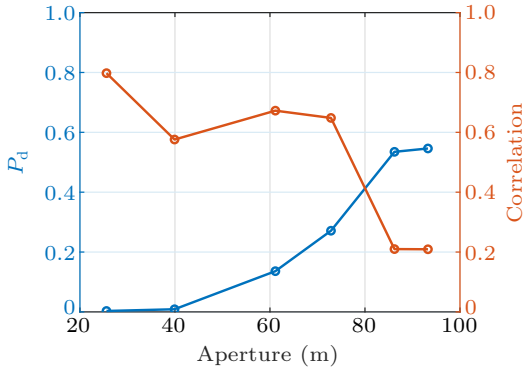


Fig. 18. Performance of the GLRD and the correlation between the direct blast and the signal under different aperture conditions with SNR = 15 dB and SDR = -30 dB.

6. Conclusion

This paper aims to achieve target detection using the forward scattering signal in uncertain shallow-water environments. To address the performance degradation or even failure of the GLRD in a known environment caused by environmental mismatches, we account for environmental uncertainties and extend the method to uncertain environments. In the bistatic sonar configuration where the source is positioned on the broadside of a large aperture HLA, the GLRD demonstrates robustness against environmental uncertainties and exhibits good resistance against the direct blast. Moreover, we demonstrate that under high-frequency conditions, GLRD performs better in detecting a target near the source-receiver baseline using forward scattering than backward scattering, as the energy of the signal scattered in the forward direction relative to the target is greater than that scattered in the backward direction.

However, although the large aperture HLA can distinguish the forward scattering signal from the direct blast, there is performance degradation in the region close to the HLA. This is because, due to the lack of prior knowledge about the scattering characteristics of a non-cooperative target, which is directional in space, we approximate the forward scattering signal as a signal radiated by a non-directional source. This

approximation leads to signal mismatch in the near field and results in performance degradation, which is the problem we aim to address in the future.

Appendix A

Assuming that the signal $\boldsymbol{s}$ is uncorrelated with the noise $\boldsymbol{w}$, there is[29]

$$\begin{aligned} E\left[(\boldsymbol{s}+\boldsymbol{w})^{\mathrm{H}}\boldsymbol{A}(\boldsymbol{s}+\boldsymbol{w})\right] &= E\left(\boldsymbol{s}^{\mathrm{H}}\boldsymbol{A}\boldsymbol{s}\right)+E\left(\boldsymbol{w}^{\mathrm{H}}\boldsymbol{A}\boldsymbol{w}\right) \\ &= \mathrm{tr}\left(\boldsymbol{A}\boldsymbol{R}_{\mathrm{s}}\right)+\mathrm{tr}\left(\boldsymbol{A}\boldsymbol{R}_{\mathrm{w}}\right), \end{aligned} \tag{A1}$$

where $\boldsymbol{R}_{\mathrm{s}}=E\left(\boldsymbol{s}\boldsymbol{s}^{\mathrm{H}}\right)$ and $\boldsymbol{R}_{\mathrm{w}}=E\left(\boldsymbol{w}\boldsymbol{w}^{\mathrm{H}}\right)$ are the spatial covariance matrix of the signal and noise, respectively. According to Eqs. (18) and (A1), the mean of the detection statistic under $\mathcal{H}_0$ and $\mathcal{H}_1$ are denoted by (the constant term $\sigma^2/2$ is omitted)

$$\begin{aligned} E\left(T|\mathcal{H}_0\right) &= \mathrm{tr}\left(\boldsymbol{A}_0\boldsymbol{R}_{\mathrm{source}}\right)+\mathrm{tr}\left(\boldsymbol{A}_0\boldsymbol{R}_{\mathrm{w}}\right), \\ E\left(T|\mathcal{H}_1\right) &= \mathrm{tr}\left(\boldsymbol{A}_1\boldsymbol{R}\right)+\mathrm{tr}\left(\boldsymbol{A}_1\boldsymbol{R}_{\mathrm{w}}\right). \end{aligned} \tag{A2}$$

To calculate the variance of the statistic, the mean of the second-order statistic is calculated first, which is denoted by

$$\begin{aligned} &E\left\{\left[(\boldsymbol{s}+\boldsymbol{w})^{\mathrm{H}}\boldsymbol{A}(\boldsymbol{s}+\boldsymbol{w})\right]^2\right\} \\ &= E\Big[\left(\boldsymbol{s}^{\mathrm{H}}\boldsymbol{A}\boldsymbol{s}\right)^2+\left(\boldsymbol{s}^{\mathrm{H}}\boldsymbol{A}\boldsymbol{w}+\boldsymbol{w}^{\mathrm{H}}\boldsymbol{A}\boldsymbol{s}\right)^2+\left(\boldsymbol{w}^{\mathrm{H}}\boldsymbol{A}\boldsymbol{w}\right)^2 \\ &\quad +2\boldsymbol{s}^{\mathrm{H}}\boldsymbol{A}\boldsymbol{s}\boldsymbol{s}^{\mathrm{H}}\boldsymbol{A}\boldsymbol{w}+2\boldsymbol{s}^{\mathrm{H}}\boldsymbol{A}\boldsymbol{s}\boldsymbol{w}^{\mathrm{H}}\boldsymbol{A}\boldsymbol{s} \\ &\quad +2\boldsymbol{w}^{\mathrm{H}}\boldsymbol{A}\boldsymbol{w}\boldsymbol{s}^{\mathrm{H}}\boldsymbol{A}\boldsymbol{w}+2\boldsymbol{w}^{\mathrm{H}}\boldsymbol{A}\boldsymbol{w}\boldsymbol{w}^{\mathrm{H}}\boldsymbol{A}\boldsymbol{s} \\ &\quad +2\boldsymbol{s}^{\mathrm{H}}\boldsymbol{A}\boldsymbol{s}\boldsymbol{w}^{\mathrm{H}}\boldsymbol{A}\boldsymbol{w}\Big]. \end{aligned} \tag{A3}$$

According to the Reed's formulas for complex Gaussian random variables,[29,32] there are

$$\begin{aligned} E\left(\boldsymbol{s}^{\mathrm{H}}\boldsymbol{A}\boldsymbol{s}\boldsymbol{s}^{\mathrm{H}}\boldsymbol{A}\boldsymbol{w}\right) &= E\left(\boldsymbol{s}^{\mathrm{H}}\boldsymbol{A}\boldsymbol{s}\boldsymbol{w}^{\mathrm{H}}\boldsymbol{A}\boldsymbol{s}\right) \\ &= E\left(\boldsymbol{w}^{\mathrm{H}}\boldsymbol{A}\boldsymbol{w}\boldsymbol{s}^{\mathrm{H}}\boldsymbol{A}\boldsymbol{w}\right) \\ &= E\left(\boldsymbol{w}^{\mathrm{H}}\boldsymbol{A}\boldsymbol{w}\boldsymbol{w}^{\mathrm{H}}\boldsymbol{A}\boldsymbol{s}\right)=0, \end{aligned} \tag{A4}$$

$$E\left[\left(\boldsymbol{w}^{\mathrm{H}}\boldsymbol{A}\boldsymbol{w}\right)^2\right] = \mathrm{tr}^2\left(\boldsymbol{A}\boldsymbol{R}_{\mathrm{w}}\right)+\mathrm{tr}\left(\boldsymbol{A}\boldsymbol{R}_{\mathrm{w}}\right)^2. \tag{A5}$$

The second term in Eq. (A3) is given by

$$\begin{aligned} &\left[\left(\boldsymbol{s}^{\mathrm{H}}\boldsymbol{A}\boldsymbol{w}+\boldsymbol{w}^{\mathrm{H}}\boldsymbol{A}\boldsymbol{s}\right)^2\right] \\ &= E\left\{\left[2\mathrm{Re}\left(\boldsymbol{s}^{\mathrm{H}}\boldsymbol{A}\boldsymbol{w}\right)\right]^2\right\} \\ &= 4E\left\{\left[\mathrm{Re}\left(\boldsymbol{s}^{\mathrm{H}}\boldsymbol{A}\right)\mathrm{Re}\left(\boldsymbol{w}\right)-\mathrm{Im}\left(\boldsymbol{s}^{\mathrm{H}}\boldsymbol{A}\right)\mathrm{Im}\left(\boldsymbol{w}\right)\right]^2\right\} \\ &= 4E\left\{\left[\mathrm{Re}\left(\boldsymbol{s}^{\mathrm{H}}\boldsymbol{A}\right)\mathrm{Re}\left(\boldsymbol{w}\right)\right]^2+\left[\mathrm{Im}\left(\boldsymbol{s}^{\mathrm{H}}\boldsymbol{A}\right)\mathrm{Im}\left(\boldsymbol{w}\right)\right]^2\right\} \\ &= 2\sigma^2\left(\left\|\mathrm{Re}\left(\boldsymbol{s}^{\mathrm{H}}\boldsymbol{A}\right)\right\|_2^2+\left\|\mathrm{Im}\left(\boldsymbol{s}^{\mathrm{H}}\boldsymbol{A}\right)\right\|_2^2\right) \\ &= 2\sigma^2\left\|\boldsymbol{A}^{\mathrm{H}}\boldsymbol{s}\right\|_2^2. \end{aligned} \tag{A6}$$

From Eqs. (A3)–(A6), the mean of the second-order statistic can be rewritten by

$$\begin{aligned} &E\left\{\left[(\boldsymbol{s}+\boldsymbol{w})^{\mathrm{H}}\boldsymbol{A}(\boldsymbol{s}+\boldsymbol{w})\right]^2\right\} \\ &= \left[\mathrm{tr}\left(\boldsymbol{A}\boldsymbol{R}_{\mathrm{s}}\right)+\mathrm{tr}\left(\boldsymbol{A}\boldsymbol{R}_{\mathrm{w}}\right)\right]^2 \\ &\quad +\mathrm{tr}\left(\boldsymbol{A}\boldsymbol{R}_{\mathrm{w}}\right)^2+2\sigma^2\left\|\boldsymbol{A}^{\mathrm{H}}\boldsymbol{s}\right\|_2^2. \end{aligned} \tag{A7}$$

Therefore, the variance of the statistic is denoted by

$$D\left[(\boldsymbol{s}+\boldsymbol{w})^{\mathrm{H}}\boldsymbol{A}(\boldsymbol{s}+\boldsymbol{w})\right] = \mathrm{tr}\left(\boldsymbol{A}\boldsymbol{R}_{\mathrm{w}}\right)^2+2\sigma^2\left\|\boldsymbol{A}^{\mathrm{H}}\boldsymbol{s}\right\|_2^2. \tag{A8}$$

According to Eqs. (18) and (A8), the variance of the detection statistic under $\mathcal{H}_0$ is denoted by (the constant term $\sigma^2/2$ is omitted)

$$D\left(T|\mathcal{H}_0\right) = \mathrm{tr}\left(\boldsymbol{A}_0\boldsymbol{R}_{\mathrm{w}}\right)^2+2\sigma^2\left\|\boldsymbol{A}_0\boldsymbol{s}_{\mathrm{source}}\right\|_2^2. \tag{A9}$$

Inserting Eqs. (A2) and (A9) into Eq. (19), the deflection coefficient is given by

$$\begin{aligned} \kappa &= \frac{E\left(T|\mathcal{H}_1\right)-E\left(T|\mathcal{H}_0\right)}{D\left(T|\mathcal{H}_0\right)^{1/2}} \\ &= \frac{\mathrm{tr}\left(\boldsymbol{A}_1\boldsymbol{R}\right)+\mathrm{tr}\left(\boldsymbol{A}_1\boldsymbol{R}_{\mathrm{w}}\right)-\mathrm{tr}\left(\boldsymbol{A}_0\boldsymbol{R}_{\mathrm{source}}\right)-\mathrm{tr}\left(\boldsymbol{A}_0\boldsymbol{R}_{\mathrm{w}}\right)}{\sqrt{\mathrm{tr}\left(\boldsymbol{A}_0\boldsymbol{R}_{\mathrm{w}}\right)^2+2\sigma^2\left\|\boldsymbol{A}_0\boldsymbol{s}_{\mathrm{source}}\right\|_2^2}} \\ &= \frac{\mathrm{tr}\left(\boldsymbol{A}_1\boldsymbol{R}\right)-\mathrm{tr}\left(\boldsymbol{A}_0\boldsymbol{R}_{\mathrm{source}}\right)}{\sqrt{\sigma^4\mathrm{tr}\left(\boldsymbol{A}_0^2\right)+2\sigma^2\left\|\boldsymbol{A}_0\boldsymbol{s}_{\mathrm{source}}\right\|_2^2}}. \end{aligned} \tag{A10}$$

Appendix B

For Eq. (19), it worth noting that both $\boldsymbol{P}_{\hat{G}_i}$ and $\boldsymbol{P}_{\hat{g}_i}$ are the idempotent Hermitian matrices, so the numerator can be rewritten as[29]

$$\begin{aligned} &\mathrm{tr}\left(\boldsymbol{A}_1\boldsymbol{R}\right)-\mathrm{tr}\left(\boldsymbol{A}_0\boldsymbol{R}_{\mathrm{source}}\right) \\ &= E\left[\left(\boldsymbol{s}_{\mathrm{source}}+\boldsymbol{s}_{\mathrm{target}}\right)^{\mathrm{H}}\left(\boldsymbol{P}_{\hat{G}_1}-\boldsymbol{P}_{\hat{g}_1}\right)\left(\boldsymbol{s}_{\mathrm{source}}+\boldsymbol{s}_{\mathrm{target}}\right)\right] \\ &\quad -E\left[\boldsymbol{s}_{\mathrm{source}}^{\mathrm{H}}\left(\boldsymbol{P}_{\hat{G}_0}-\boldsymbol{P}_{\hat{g}_0}\right)\boldsymbol{s}_{\mathrm{source}}\right] \\ &= \max_{C}\left\|\boldsymbol{P}_G\left(\boldsymbol{s}_{\mathrm{source}}+\boldsymbol{s}_{\mathrm{target}}\right)\right\|_2^2 \\ &\quad -\max_{C_{\mathrm{source}}}\left\|\boldsymbol{P}_g\left(\boldsymbol{s}_{\mathrm{source}}+\boldsymbol{s}_{\mathrm{target}}\right)\right\|_2^2 \\ &\quad -\max_{C}\left\|\boldsymbol{P}_G\boldsymbol{s}_{\mathrm{source}}\right\|_2^2+\max_{C_{\mathrm{source}}}\left\|\boldsymbol{P}_g\boldsymbol{s}_{\mathrm{source}}\right\|_2^2. \end{aligned} \tag{B1}$$

Additionally, for the denominator, there is

$$\begin{aligned} \mathrm{tr}\left(\boldsymbol{A}_0^2\right) &= \mathrm{tr}\left(\boldsymbol{P}_{\hat{G}_0}\right)+\mathrm{tr}\left(\boldsymbol{P}_{\hat{g}_0}\right)-2\mathrm{tr}\left(\boldsymbol{P}_{\hat{G}_0}\boldsymbol{P}_{\hat{g}_0}\right) \\ &= 3-2E\left(\hat{\boldsymbol{g}}_0^{\mathrm{H}}\boldsymbol{P}_{\hat{G}_0}\hat{\boldsymbol{g}}_0\right)/\left\|\hat{\boldsymbol{g}}_0\right\|_2^2 \\ &= 3-2\left\|\boldsymbol{P}_{\hat{G}_0}\hat{\boldsymbol{g}}_0\right\|_2^2/\left\|\hat{\boldsymbol{g}}_0\right\|_2^2. \end{aligned} \tag{B2}$$

Taking both Assumptions 1 and 2 into account, $\hat{\boldsymbol{g}}_0$ and $\hat{\boldsymbol{G}}_1$ can be denoted by

$$\hat{\boldsymbol{g}}_0=\hat{\boldsymbol{g}}\left(\boldsymbol{\Phi},\boldsymbol{r}_{\mathrm{s}}\right)|\mathcal{H}_0=\boldsymbol{g}\left(\boldsymbol{\Phi},\boldsymbol{r}_{\mathrm{s}}\right),$$

$$\hat{\boldsymbol{G}}_1 = \hat{\boldsymbol{G}}|\mathcal{H}_1 = \left[\boldsymbol{g}\left(\boldsymbol{\Phi}, \boldsymbol{r}_{\mathrm{s}}\right), \boldsymbol{g}\left(\boldsymbol{\Phi}, \boldsymbol{r}_{\mathrm{t}}\right)\right], \tag{B3}$$

and for the numerator of Eq. (19), there are

$$\begin{aligned} &\max_{C} \left\| \boldsymbol{P}_G \left(\boldsymbol{s}_{\text{source}} + \boldsymbol{s}_{\text{target}}\right)\right\|_2^2 = \left\|\boldsymbol{s}_{\text{source}} + \boldsymbol{s}_{\text{target}}\right\|_2^2, \\ &\max_{C} \|\boldsymbol{P}_G \boldsymbol{s}_{\text{source}}\|_2^2 = \max_{C_{\text{source}}} \left\|\boldsymbol{P}_g \boldsymbol{s}_{\text{source}}\right\|_2^2 = \|\boldsymbol{s}_{\text{source}}\|_2^2. \end{aligned} \tag{B4}$$

Meanwhile, for the denominator of Eq. (19), there are

$$\mathrm{tr}\left(\boldsymbol{A}_0^2\right) = 3 - 2\left\|\boldsymbol{P}_{\hat{G}_0} \boldsymbol{s}_{\text{source}}\right\|_2^2 / \|\boldsymbol{s}_{\text{source}}\|_2^2 = 1, \tag{B5}$$

$$\|\boldsymbol{A}_0 \boldsymbol{s}_{\text{source}}\|_2^2 = \left\|\boldsymbol{P}_{\hat{G}_0} \boldsymbol{s}_{\text{source}} - \boldsymbol{P}_{\hat{g}_0} \boldsymbol{s}_{\text{source}}\right\|_2^2 = 0. \tag{B6}$$

Therefore, Eq. (19) can be further simplified to

$$\kappa = \frac{\left\|\boldsymbol{s}_{\text{source}} + \boldsymbol{s}_{\text{target}}\right\|_2^2 - \max\limits_{C_{\text{source}}} \left\|\boldsymbol{P}_g \left(\boldsymbol{s}_{\text{source}} + \boldsymbol{s}_{\text{target}}\right)\right\|_2^2}{\sigma^2}. \tag{B7}$$

Acknowledgment

Project supported by the National Natural Science Foundation of China (Grant No. 12004335).

References

[1] Morse P M and Ingard K U 1968 *Theoretical Acoustics*, 1st edn. (New York: McGraw-Hill), pp. 400–441

[2] Naluai N K, Lauchle G C, Gabrielson T B and Joseph J H 2007 *J. Acoust. Soc. Am.* **121** 1909

[3] Lei B, Yang K D and Ma Y L 2010 *Chin. Phys. B.* **19** 054301

[4] Glaser J I 1985 *IEEE Trans. Aerosp. Electron. Syst.* **AES-21** 70

[5] Matveev A L, Spindel R C and Rouseff D 2007 *IEEE J. Ocean. Eng.* **32** 626

[6] Lei B, Ma Y L and Yang K D 2011 *Chin. Phys. Lett.* **28** 034302

[7] Lei B, He Z Y and Zhang R 2021 *Acta Phys. Sin.* **70** 224302 (in Chinese)

[8] He Z Y, Lei B and Yang Y X 2023 *Acta Phys. Sin.* **72** 144301 (in Chinese)

[9] Song H, Kuperman W A, Hodgkiss W S, Akal T and Guerrini P 2003 *IEEE J. Ocean. Eng.* **28** 246

[10] Sabra K G, Conti S, Roux P, Akal T, Kurperman W A, Stevenson J M, Tesei A and Guerrini P 2010 *J. Acoust. Soc. Am.* **127** 3430

[11] Lei B, Yang Y X, Yang K D and Ma Y L 2017 *J. Acoust. Soc. Am.* **141** 1704

[12] Lei B, He Z Y, Yang Y X, Sun C and He C L 2022 *Appl. Acoust.* **190** 108635

[13] Lei B, He Z Y, Fan Q G and Yang Y X 2025 *Appl. Acoust.* **239** 110856

[14] Gao F, Xu F H, Li Z L, Qin J X and Zhang Q Y 2023 *Chin. Phys. B.* **32** 034302

[15] Mo Y X, Zhang C J, Lu L C, Sun Q H and Ma L 2024 *Chin. Phys. B.* **33** 034301

[16] Sha L W and Nolte L W 2005 *J. Acoust. Soc. Am.* **117** 1942

[17] Li M Y, Sun C and Willett P 2018 *IEEE J. Ocean. Eng.* **43** 131

[18] Li M Y, Sun C, Zhao H F and Willett P 2022 *IEEE J. Ocean. Eng.* **47** 201

[19] Kay S M 1998 *Fundamentals of Statistical Signal Processing Volume II: Detection Theory* (Prentice Hall) p. 197-205+473-478

[20] Collins M D and Kuperman W A 1991 *J. Acoust. Soc. Am.* **90** 1410

[21] Li M Y, Sun C and Shao X 2014 *Acta Phys. Sin.* **63** 204302 (in Chinese)

[22] Lei B, He Z Y, Zhang Y and Yang Y X 2022 *Digit. Signal Process.* **129** 103657

[23] Wang X, Sun C and Li M Y 2023 *J. Acoust. Soc. Am.* **153** 2909

[24] Luo J H, Sun C and Li M Y 2024 *J. Mar. Sci. Eng.* **12** 1864

[25] Ingenito F 1987 *J. Acoust. Soc. Am.* **82** 2051

[26] Makris N C 1998 *J. Acoust. Soc. Am.* **104** 2105

[27] Jensen F B, Kuperman W A, Porter M B and Schmidt H 2011 *Computational Ocean Acoustics*, 2nd edn. (New York: Springer), pp. 337–380+420

[28] Porter M B and Tolstoy A 1994 *J. Comput. Acoust.* **2** 161

[29] Morgan D R and Smith T M 1990 *J. Acoust. Soc. Am.* **87** 737

[30] Ye Z, Hoskinson E, Dewey R K, Ding L and Farmer D M 1997 *J. Acoust. Soc. Am.* **102** 1964

[31] Skolnik M I 2008 *Radar Handbook*, 3rd edn. (New York: McGraw-Hill) p. 23.21

[32] Reed I S 1962 *IRE Trans. Inf. Theory* **8** 194